

On estimating angular momenta of infalling protostellar cores from observations

Shangjia Zhang¹, Lee Hartmann¹ *, Manuel Zamora-Avilés^{1,2}, and Aleksandra Kuznetsova¹

¹*Department of Astronomy, University of Michigan, 1085 S. University Ave, Ann Arbor, MI 48109 USA*

²*Instituto de Radioastronomía y Astrofísica, Universidad Nacional Autónoma de México, Apdo. Postal 72-3 (Xangari), Morelia, Michocán 58089, México*

Accepted XXX. Received YYY; in original form ZZZ

ABSTRACT

We use numerical simulations of molecular cloud formation in the colliding flow scenario to investigate the reliability of observational estimates of the angular momenta of early-state, low-mass protostellar cores. We show that, with suitable corrections for projection factors, molecular line observations of velocity gradients in NH₃ can be used to provide reasonable estimates of core angular momenta within a factor of two to three, with a few large underestimates due to unfavorable viewing angles. Our results differ from previous investigations which suggested that observations might overestimate true angular momenta by as much as an order of magnitude; the difference is probably due to the much smoother velocity field on small scales in our simulations, which result from allowing turbulence to decay and gravitational infall to dominate. The results emphasize the importance of understanding the nature of “turbulent” velocities, with implications for the formation of protostellar disks during core collapse.

Key words: turbulence, magnetic fields – stars: formation – ISM: clouds – ISM: structure – ISM: kinematics and dynamics

1 INTRODUCTION

The angular momenta of collapsing protostellar clouds establish the properties of binary and multiple stars and the initial conditions of their protoplanetary disks. Recent observations have demonstrated that disks of appreciable size can form early, during the Class I and even the Class 0 protostellar phases (Tobin et al. 2012; Ohashi et al. 2014; Aso et al. 2015; Yen et al. 2015; Oya et al. 2016; see Takakuwa et al. 2017 for a review). However, simulations of collapsing magnetized protostellar cores over the last few years have indicated that magnetic fields can in some circumstances remove so much angular momentum that large disks do not form (see, e.g. Seifried et al. 2013; Li et al. 2014, for reviews). Ambipolar diffusion can play a crucial role in reducing the magnetic flux responsible for angular momentum transport outward (Masson et al. 2016; Vaytet et al. 2018), although it is unclear whether it is sufficient to allow the formation of disks during the Class 0 phase (Dapp et al. 2012). Alternatively, substantial misalignment of the magnetic field rela-

tive to the net rotation axis, and/or diffusion of the field in a turbulent environment, can allow early disk formation (Joos et al. 2012, 2013; Santos-Lima et al. 2012, 2013; Seifried et al. 2012, 2013; Krumholz et al. 2013; Lewis et al. 2015; Wurster et al. 2016, 2017). In view of the theoretical uncertainties, observational estimates of infalling protostellar core angular momenta (and their directions) can be useful. Following the classic work by Goodman et al. (1993) on the rotation of protostellar cores, additional observational estimates of angular momenta have been made (Caselli et al. 2002) (see the review by Belloche 2013), with added emphasis on the angular momenta of inner envelopes (Yen et al. 2015) to help constrain disk formation.

However, numerical simulations by Offner et al. (2008) and Dib et al. (2010) suggest that observations can overestimate true angular momenta by as much as a factor of 10. These large bias factors presumably result from the assumed complexity of the turbulent velocity field, which cancels out some of the angular momentum on small scales that is smoothed out on large scales with the usual observational procedures. This interpretation is supported by the results of Offner et al. indicating that the bias is smaller if the ini-

* E-mail: lhartm@umich.edu

tial seeded turbulent velocity field is allowed to decay rather than be continuously driven.

The approach to developing initial conditions that we favor is one in which the turbulence is the result of cloud formation, followed by gravitational collapse (e.g., Heitsch et al. 2006; Ballesteros-Paredes et al. 2011). The supersonic velocity fields at the time of star (sink particle) formation are then the result (mostly) of overdensities in the cloud which drive motion gravitationally. This arguably results in a smoother velocity field than in the case of continued driving of turbulence by some unspecified mechanism; in turn, this could mean that observational estimates of angular momenta could be more representative of true values. To investigate this further, in this paper we employ the results of numerical simulations for dense cores, post-process them with radiative transfer, and use the same methods of analysis for closer comparison with observational results.

2 NUMERICAL METHODS

2.1 Numerical simulations with FLASH

The sub-parsec cores analyzed in this work come from numerical simulations at a much bigger scale (256 pc) presented in Zamora-Avilés et al. (2018, model labeled B3J). This simulation was carried out with the Eulerian adaptive mesh refinement code FLASH (version 2.5; Fryxell et al. 2000) with the objective of studying the effect of magnetic fields in the formation and evolution of molecular clouds (MCs). In that work, the simulated clouds are assembled by two warm neutral streams (or inflows), which collide at the center of the numerical box. The collision compresses the warm gas triggering a phase transition due to the thermal instability (Field 1965), thus producing cold gas. Moreover, the converging flows through different dynamical instabilities inject naturally the turbulence that characterizes MCs (see, e.g., Heitsch et al. 2006), which in turn produce the overdensities (seeds of cores). As the cold layer continues accreting material from the inflows, it increases its mass and column density, allowing the formation of molecular gas, and eventually the entire cloud enters in a state of hierarchical collapse (see, e.g., Hartmann et al. 2001).

The simulation includes the relevant physical processes for cloud formation/evolution such as heating and cooling, self-gravity, magnetic fields, and sink formation. We also ran another simulation with identical initial conditions but with no magnetic field for comparison. In the simulation with magnetic fields we use an ideal MHD treatment in which the equations are solved using the MHD HLL3R solver (e.g., Waagan et al. 2011), which is suitable for highly supersonic astrophysical flows. The heating/cooling process are implemented using the analytic fits by Koyama & Inutsuka (2002) for the heating and cooling functions, which are based in the thermal and chemical calculations considered by Wolfire et al. (1995); Koyama & Inutsuka (2000). The gas self-gravity is implemented using the Tree-based technique (e.g., Wünsch et al. 2018) and we also consider the gravitational interactions between sink particles (see below) and gas cells. For further information, we refer to the reader to Zamora-Avilés et al. (2018).

As we are interested in following the gravitational collapse of cores, we refine according to the Jeans criterion,

resolving the local Jeans length by at least 10 grid cells in order to prevent spurious fragmentation (Truelove et al. 1997).¹ When the maximum resolution is reached and the Jeans length of the collapsing gas can no longer be resolved, we introduce sink particles (Federrath et al. 2010). Note, however, that the original simulations refine only 10 levels, reaching a spatial resolution of 0.03 pc which just marginally resolves the dense molecular cores. Thus, in order to resolve the structure within cores, we re-ran the simulation (just a few tenths of Myr before sink formation) allowing the code to refine a further eight levels within a radius of ~ 5 pc of each sink, reaching thus an effective resolution of ~ 25 AU (1.2×10^{-4} pc). We let each core evolve until they start to form sinks at a threshold density of $n_{\text{thr}} \approx 2.2 \times 10^9 \text{ cm}^{-3}$.

The initial conditions are as follows. Each stream is cylindrical, with 32 pc in radius and 112 pc in length along the x-direction, containing warm gas in thermal equilibrium with density $n = 2 \text{ cm}^{-3}$ and temperature $T=1450$ K. These streams are completely contained in the numerical box of size 256 pc in the x-axis and 128 pc in the y/z-axes. The streams collide at a transonic velocity of $\sim 7.5 \text{ km s}^{-1}$, and we impose a background turbulent velocity field (with Mach number of 0.7) in order to trigger the dynamical instabilities in the shocked layer. In the MHD simulation, the magnetic field is initially uniform along the x-direction with a strength of $3 \mu\text{G}$. This corresponds to an initial mass-to-flux ratio, μ , of 1.5 times the critical value (μ_{crit}), and thus the cloud is magnetically super-critical as a whole. We find that the mass-to-flux ratios for the cores at the time we analyze them are roughly critical on scales of 2×10^4 AU, with the exact values depending upon the scale analyzed (because there is generally significant mass on large scales).

Panel 1 of Fig. 1 shows the edge-on column density (N) of the entire MC at $t \approx 11.5$ Myr.² At this time we restarted the simulation for a few tenths of Myrs more, zooming, for instance, around the first star-forming core. Panels 2-4 of the same figure show projections of this core at $t \approx 11.68$ Myr in increasingly smaller boxes.

2.2 Post-processing

We made cutouts from the simulation data cubes for ten isolated cores from both the MHD and HD simulations. The masses of these cores and sinks are listed in Table 1. The cutouts were cubes of length 0.2, 0.1 and 0.05 pc to analyze the properties as a function of scale. For each cubical cutout, the gas properties (density, velocity and temperature) were interpolated on 64^3 uniform grids centered on the sinks. The gas velocities were transformed into the rest frame of the sink, except for the low-mass sinks in Core 4, 8 and 16 which are moving much faster than the surrounding gas, and so we used the rest frame velocity of the calculation. (Presumably these sinks have been gravitationally scattered by nearby high-mass sinks.) The temperatures were taken

¹ Note that the Truelove criterion requires the local Jeans length to be resolved by at least four cells in HD simulations. However, in MHD ten cells are a good compromise to properly follow the magnetic field amplification by gravity-driven turbulence (Federrath et al. 2011).

² Note that the MC extends several tens of pc.

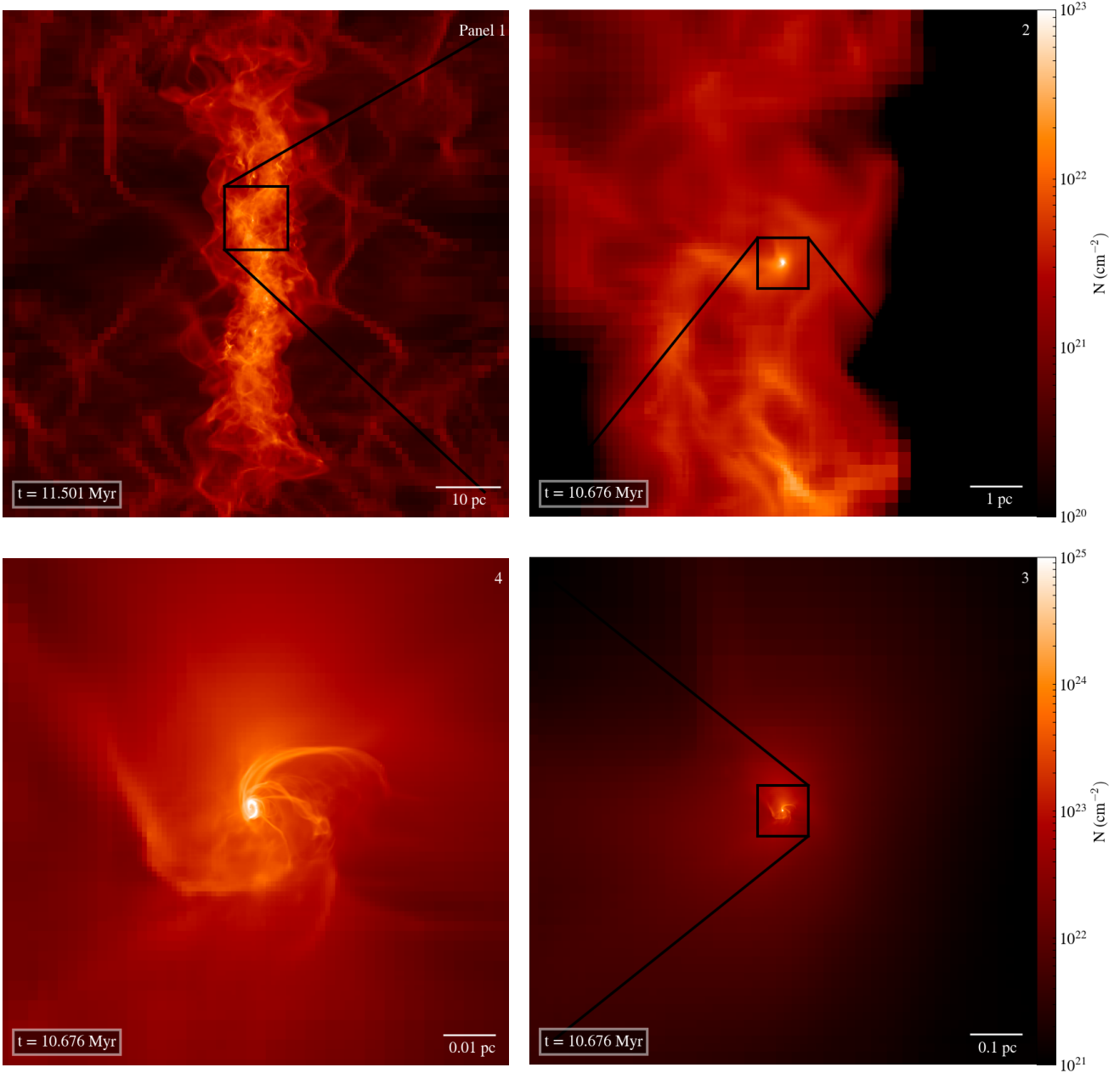


Figure 1. Edge-on column density maps. Panel 1 shows the whole MC at $t \approx 11.5$ Myr for the MHD simulation. At this time, we restarted the simulation (for a few tenths of Myr more), zooming into the first star-forming core. Panels 2, 3, and 4 show this core in a box size of 10, 1, and 0.1 pc, respectively. Note that the color bar scale is different in the upper and lower panels. This figure was generated using the python-based `yt` toolkit (Turk et al. 2011).

from the simulation results and are in the range $\sim 9 - 13$ K. This ignores heating by the central protostar, but this should be quite minimal on the scales we consider for typical protostellar luminosities. The simulation data in the cutouts are available upon request.

These cutouts were then used as input to the LIME (Brinch & Hogerheijde 2010) radiative transfer code to produce channel maps of the NH_3 (1,1) inversion lines in three orthogonal projections. The velocity resolution between neighboring channels was set to be 0.1 km s^{-1} . The channel maps were made in three orthogonal projections de-

noted XY , XZ and YZ , on the four different scales of the cutouts.

We do not include chemical modeling in our analysis. Initially, we set the abundance of NH_3 relative to H_2 to a uniform and relatively high value of 8×10^{-8} (Aikawa & Herbst 1999). We also calculated emission maps using a lower abundance for NH_3 of 5×10^{-9} ; this did not change the results of the velocity analysis significantly. In addition, we examined the effect of setting the ammonia abundances to zero at densities below 10^4 cm^{-3} , as studies of nearby cores indicate that bright NH_3 emission generally occurs at higher densities (e.g., Myers & Benson 1983). Again, this made no

Table 1. Masses of sinks and enclosed gas masses M_{\odot} as a function of the radius in AU.

Core	M_{sink}	M_{5000}	M_{10000}	M_{20000}
1	2.7	4.0	7.5	12.8
2	0.7	3.9	8.2	15.9
3	1.2	3.2	6.4	11.2
4	0.3	4.2	7.3	10.8
5	0.9	3.1	6.2	11.1
6	0.03	5.3	10.6	19.7
7	1.0	4.1	8.5	19.5
8	0.2	4.2	8.3	14.8
9	0.7	3.1	6.0	10.5
16	0.2	3.3	6.1	10.1
nonB 1	0.046	4.6	8.4	13.9
nonB 2	0.49	4.9	8.8	13.8
nonB 3	0.50	3.3	7.5	13.9
nonB 4	4.9×10^{-4}	3.6	7.0	12.5
nonB 5	5.9×10^{-3}	3.4	6.6	11.4
nonB 6	0.54	3.6	7.0	13.6
nonB 7	0.47	2.2	5.1	12.2
nonB 8	2.7×10^{-5}	5.8	12.9	23.4
nonB 9	0.55	3.9	7.1	11.9
nonB 10	0.088	4.9	10.1	15.9

significant difference to the results, especially because all of the grid cells within a radius of 5000 AU of the sinks have densities above 10^4cm^{-3} .

For each cutout, we used the Python package `spectral_cube` (Robitaille et al. 2016) to make moment maps (intensity maps, intensity-weighted velocity maps and linewidth maps, or moment 0, 1 and 2 respectively) and the Python package `pvextractor` (Ginsburg et al. 2016) to make position-velocity (p-v) diagrams. The p-v diagrams were made by slicing along the direction of the velocity gradients measured on the various scales (see §2.3).

The radiative transfer solutions have convergence problems for some cores, such as Core 2. We believe that this is due to the limitation of LIME’s linear interpolation scheme for the velocity field. Problems arise when the velocity differences between neighbor cells are greater than the turbulent velocity dispersion (Brinch, personal communication). Smoothing our complex supersonic velocity fields with a 3-D Gaussian kernel did not help solve the problem. The only method we found to promote satisfactory convergence in the problem cases with the current version of LIME and our computational resources was to increase the turbulent velocity “doppler” parameter from 0.2 km s^{-1} to 0.8 km s^{-1} . To see whether this smoothing has a significant effect on our results, we also generated moment maps with simple volume density-weighted “emission” to be analyzed in the same way as the maps generated with LIME. As discussed in the results section, while there are significant differences in some projections for a few cores, the overall velocity gradient results did not change.

2.3 Velocity gradient analysis

We fit for the “observed” velocity gradient using the method that Goodman et al. (1993) adopted to measure ammonia observations of cores. The method involves 3-D least square

fitting of the moment 1 map with the following equation:

$$v_{LSR} = v_0 + a\Delta x + b\Delta y, \quad (1)$$

where v_{LSR} is the velocity at each pixel, v_0 is the average velocity over the map (relative to the sink), a and b are the fitting parameters, and Δx and Δy are the displacements on x-axis and y-axis, where x and y are the displacements perpendicular to the particular line of sight in the map. The mean angular velocity is then

$$\Omega = \sqrt{a^2 + b^2} \quad (2)$$

in units of $\text{km s}^{-1}\text{pc}^{-1}$. The position angle of the velocity gradient is then given by

$$\theta = \tan^{-1}\left(\frac{b}{a}\right). \quad (3)$$

The χ^2 statistic was used to optimize a and b ,

$$\chi^2(a, b) = \sum_i \left(\frac{v_{LSR} - f(x_i, y_i | a, b)}{\sigma_{v_{LSR}, i}} \right)^2. \quad (4)$$

The uncertainty of the velocity in the fitting was estimated following at each pixel Landman et al. (1982);

$$\sigma_{v_{LSR}} = 1.15 \left(\frac{\sigma_T}{T} \right) (\delta_v \Delta v)^{1/2} \quad (5)$$

where (T/σ_T) can be treated as the signal to noise ratio (SNR). We assume $\text{SNR} = 5$ and constant over the moment 1 map. The parameter δ_v is the linewidth (moment 2) map, and Δv is the size of the velocity bin, set to 0.1 km s^{-1} . A least square fitting method (Eq. 4) was used to find the best fit-values of a and b .

The velocity gradients were calculated on four different scales: 2500 AU, 5000 AU (0.025 pc), 10000 AU (0.05 pc) and 20000 AU (0.1 pc) in radius (half of the box length). We calculated NH_3 maps for all the four scales and the three main projections.

2.4 Specific angular momenta

The velocity gradient measurements were used to make estimates of the specific angular momentum with the assumption of solid body rotation and spherically-symmetric density profile, characterized by parameter p ,

$$j_{2D} = pR^2\Omega, \quad (6)$$

where j_{2D} denotes the observationally-inferred specific angular momentum, R is the radius of the map that is analyzed, and p is related to α in the radial density profile, which can be calculated by integrating the moment of inertia of a sphere with density profile characterized by α . If the density profile is a power-law,

$$\rho \propto r^{-\alpha}, \quad (7)$$

the relation between p and α is

$$p = \frac{2(3 - \alpha)}{3(5 - \alpha)}. \quad (8)$$

For a singular isothermal sphere, with $\alpha = 2$, $p = 2/9$, while for a uniform density sphere $p = 2/5$.

The true (mass-averaged) specific angular momenta

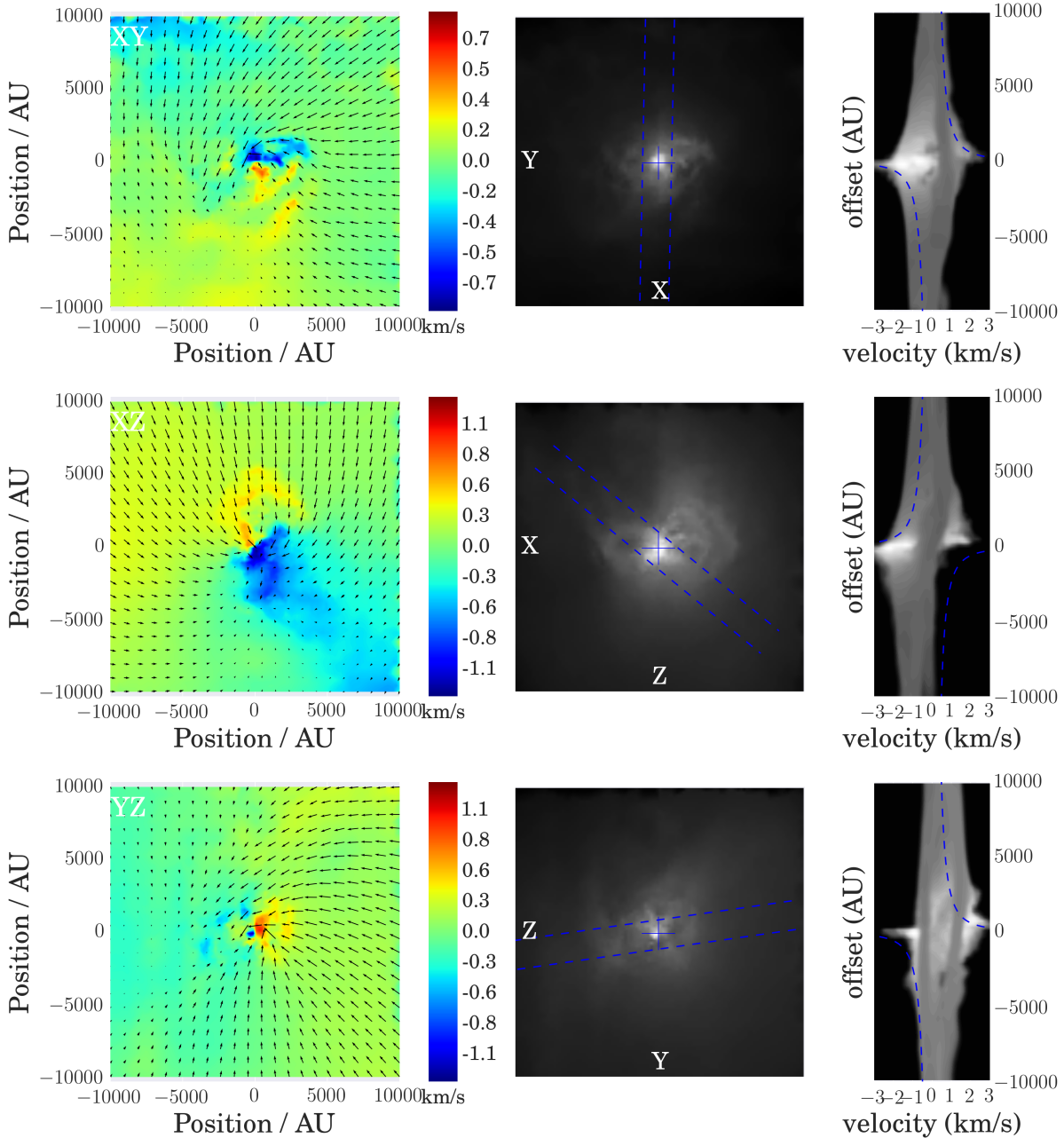


Figure 2. Moment maps and p-v diagram for Core 1 on a 0.1 pc scale. The nine panels show the comparable data for the simulation core in three projections (XY , XZ and YZ), with the left panels showing the moment 1 radial velocities in color (and velocity vectors in the plane of the sky), the center panels showing the moment 0 NH_3 map with dashed blue lines showing directions of fitted velocity gradient. The right panels are position-velocity map taken along the direction with certain width found from the velocity gradient fitting, indicated by the dashed blue lines. The dotted curves in the right panels are the Keplerian rotation velocity given the sink mass. For XY projection, the positive offset is from the upper region of the image, for XZ projection, the positive offset is from the lower right region and for YZ projection, the positive offset is from the right region of the image.

were calculated numerically within cutouts at the different scales (cubic boxes) as

$$j_{3D} = |\mathbf{J}/M| = \frac{\sum(\mathbf{r}_i \times \mathbf{v}_i)m_i}{\sum m_i}, \quad (9)$$

where \mathbf{r}_i is the distance between the sink and the gas cell and m_i and \mathbf{v}_i are the mass and velocity at each cell.

It is instructive to compare the angular momenta of our cores with some estimate of the maximum values possible

while still remaining gravitationally-bound. There is no single way of defining such maxima for objects in non-uniform rotation with arbitrary and complex density and velocity distributions, as is the case here. As a benchmark we adopt the results for the Mestel disk (Mestel 1963). This choice is motivated by two factors: first, a maximally-rotating cloud should be highly flattened; and second, the mass of the Mestel disk grows linearly with the radius, roughly consistent with the behavior of our cores (§3). Thus we use the simple

relation (for the formally infinite disk) $v^2 = GM(r)/r$, where $M(r)$ is the mass interior to r ; thus

$$j_{max} = 0.5(GM(r)r)^{1/2}, \quad (10)$$

where we use $M(r) = M_s + M_g(r)$, with M_s and M_g being the sink mass and gas mass, respectively. (The sinks have negligible angular momentum.)

3 RESULTS

3.1 Synthetic observations

Fig. 2 shows a typical example of the projected synthetic observation with NH_3 line emission (Core 1 on the 0.1 pc / 20000 AU scale in diameter). The density-weighted velocity vectors in the plane of the sky are overplotted on the moment 1 maps. The sink (protostar) is located at (0,0,0) and denoted by a cross in the moment 0 maps. The dashed lines indicate regions where the p-v diagrams were sliced, with the directions given by the velocity gradients.

The dotted lines in p-v diagrams for each orthogonal projection indicate the Keplerian rotation curve given the sink mass. While these curves qualitatively resemble the shapes in the p-v diagrams, they underestimate the observed velocity range, not only due to projection effects but because the envelopes contain significant mass beyond that of the central sink.

3.2 Observationally-inferred vs. true specific angular momenta

Figure 3 shows results for the high NH_3 abundance case. The filled circles are the estimated angular specific angular momenta for each projection of the ten cores adopting $p = 2/5$. In most cases there is reasonable agreement with the median j_{3d} angular momenta of the cores (red curve) and the range is also fairly consistent with the one-sigma dispersion (shaded area). There are a few cases where the observations strongly underestimate the median j_{3d} angular momentum, and these are due to projection effects (e.g., the line of sight is close to the orientation of the angular momentum vector). The true specific angular momenta fall well below our simple upper limit estimate (yellow curve and dark shaded area), except at the smallest scales where rotational support is most important. At scales beyond 3000 AU the slope of the upper limit is close to unity. This is consistent with the variation of enclosed mass with radius; as shown in in Fig.4, $M(r) \approx r$, so that the expected upper limit $j_{max} \propto (GMr)^{1/2} \propto r$.

Both the median j_{2d} and j_{3d} values are results are consistent with the results of Goodman et al. (1993) at 20,000 AU, as well as those of Yen et al. (2015) on 1000 AU scales. but lie above the IRAM 04191 results of Belloche et al. (2002); Belloche & André (2004) and the N_2H^+ measurements of Caselli et al. (2002), although some of the objects in the Caselli et al. sample are starless cores which are not directly comparable to our cores with sinks.

Note that the radial dependence of j_{3d} in Figure 3 demonstrates that $\Omega(r)$ is not constant but declines with increasing radius. Nevertheless, the velocity gradient method, which assumes constant angular velocity, can still yield a reasonable estimate of the actual angular momentum in most

cases. This may be due to the total angular momentum being dominated by the motion on the largest scales.

It is also of some interest to consider the reliability of observed position angles of rotation. In Fig. 5 we show a histogram of the difference in position angle between the projected velocity gradient and the projected direction of the true angular momentum vector, calculated for the ten MHD cores on the four different scales. The direction between the velocity gradient and projected j_{3D} peaks at around 90° which would indicate complete agreement between true and inferred projected position angles, but there is a dispersion around this value of about 45° , and in about 10% of the cores (those with $PA > 270^\circ$ the sense of the rotation is opposite that of the true direction (using a right-hand rule).

3.3 Sensitivity to radiative transfer

As noted in §2.2, in some cases we had to increase the turbulent velocity to unrealistically high values in order to obtain convergence for the NH_3 radiative transfer solutions. To test the sensitivity of our findings to the transfer approximations, we constructed moment maps that were simply density-weighted. As shown in Figure 6, there is little difference with and without radiative transfer solutions, indicating that the main findings are robust. There are of course significant differences in individual cases, as shown in Figure 7; even so, the estimated velocity gradients generally agree within a factor of two, which is comparable to the spread in estimated angular momentum in either case. Again, there are extended tails in the gradient and position angle differences, emphasizing that the observation of any single core in a particular projection is subject to significant uncertainties due to the complex geometry of the velocity field.

3.4 Non-magnetic simulation

We have also performed the same analysis for ten cores for the non-magnetic field simulation with the same size cutouts of the cores. The results shown in Figure 8 again show very similar behavior to that seen for the magnetic cores, except that the dispersions are larger and there are more projections with very small apparent angular momenta. This seems to be due to the sinks with very small masses, resulting from their later formation (Zamora-Avilés et al. 2018). In essence, these very low-mass objects are the equivalent of “starless cores” and so are qualitatively different than the other cores with significant central gravitating masses.

Given the similarity of the magnetic and non-magnetic runs, we examine whether the presence of the magnetic field affects the directions of the core angular momenta. Figure 9 shows a histogram of the angle between the true angular momentum vectors and the x-axis - which is the direction of the initial magnetic field. The differences are consistent with a random orientation, indicating that the magnetic field is not playing a major role in ordering the spins of the cores.

4 DISCUSSION

Our results differ from the findings of the simulations of Dib et al. (2010) and the driven simulations of Offner et al. (2008), who found that the j_{2D} is generally about 10 times

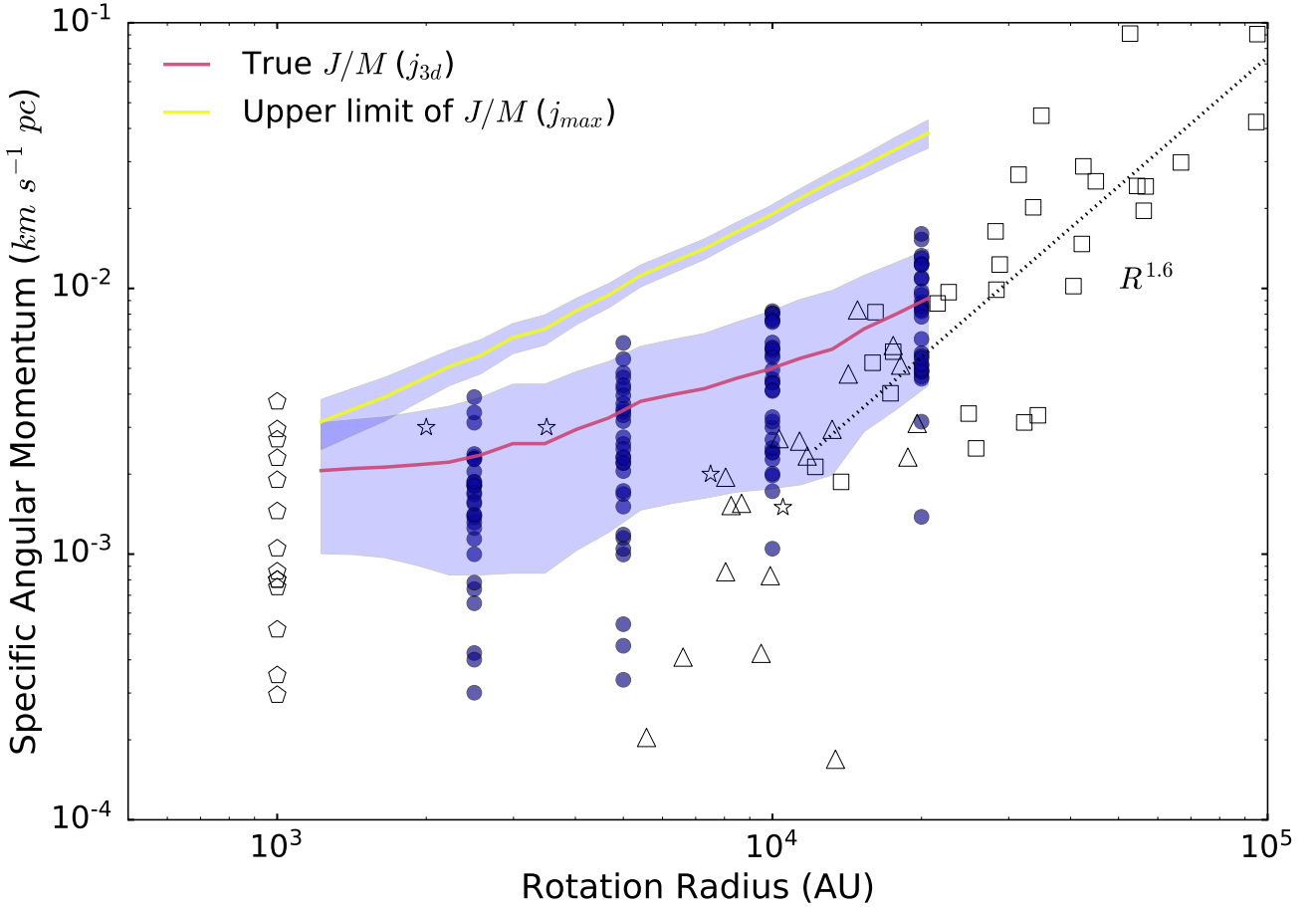


Figure 3. Specific angular momentum (J/M) as a function of radius for our ten MHD cores and a sample of observations. The circles are j_{2D} derived from observing and analyzing the simulation in the same way as was done for the real cores. The lower solid (red) curve is the median of j_{3D} for our ten cores and the light shaded area indicates $\pm 1\sigma$ (linear). The yellow curve is our estimate of the maximum j consistent with gravitational binding (equation 10) with the darker shaded area the 1σ dispersion. The squares are observations of NH_3 dense cores (Goodman et al. 1993); the stars are measurements for IRAM 04191 at four different scales (Belloche et al. 2002; Belloche & André 2004), the triangles are N_2H^+ measurements in (Caselli et al. 2002), and the pentagons are C^{18}O measurements of cores on 1000 AU scales from (Yen et al. 2015). The dotted line indicates the $r^{1.6}$ dependence of j estimated by Goodman et al. (1993).

higher than j_{3D} . We argue that this is probably due to the more complex velocity fields in those simulations than in ours, in which we allow turbulence to decay for a considerable period of time. This suggestion is consistent with the findings of Offner et al. (2008), who found that their simulation with decaying turbulence led to a much smaller bias in observationally-estimated angular momentum.

The reason for our disagreement with the results of Dib et al. (2010) is somewhat less clear, as those simulations did not include continued driving; however, we suggest that their simulations probably did have more small-scale turbulence. The Dib et al. results refer to a relatively early stage of the collapse, at ~ 0.4 free-fall times; and it seems plausible that, although the input turbulent velocity field was decaying, it still dominated the small scale motions. In support of this interpretation, we note that Dib et al. found that the Mach number of the turbulence increases at later times due to collapse in the cores, so we suggest that this is signature of gravitationally-driven turbulence rather than a remnant of the initial imposed velocity field. In our simula-

tions, which address later stages of collapse with the buildup of significant amounts of mass in the sinks, it is clear that gravity is the main driver of the supersonic motions, which apparently results in a supersonic velocity field that, while complex, does not strongly bias observational estimates. In any case, for the stage of evolution considered here, we find no support for the suggestion of Dib et al. that the global gradient method with the assumption of uniform rotation generally will result in large overestimates of specific angular momentum.

Using an appropriate value of the “fudge factor” p , we find that our “observational” estimates of the specific angular momentum fall below the maximum set by gravitational binding. One might think that if observational estimates generally indicated values that were too high by an order of magnitude, that would show up as an apparent finding that the cores wouldn’t seem to be bound. Of course we have the advantage that our $M(r)$ values are exact rather than observationally estimated as well, but such a large general discrepancy might be noticed.

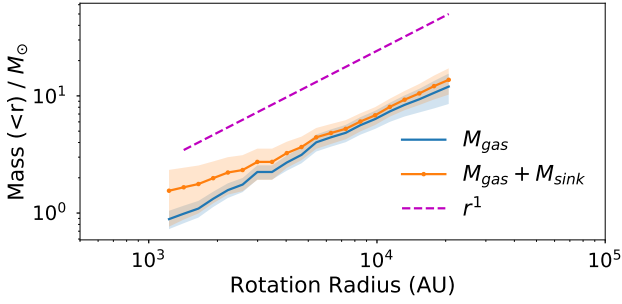


Figure 4. Cumulative mass of ten MHD cores. The solid line indicates the median of cumulative gas mass for ten cores and the dot-solid lines indicates the median of cumulative gas mass plus the sink mass. The general trend is nearly $M(r) \propto r$, except at small radii where the sink mass dominates.

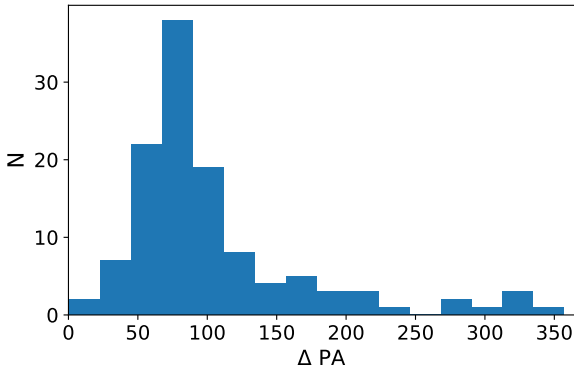


Figure 5. The distribution of the angle between the velocity gradient and the projected j_{3D} . The difference in position angle peaks at 90° , as would be the case for perfect alignment; about 25% of the cores show differences of more than 45° , with about 10% of the cores deviating by more than 90° . This is due to the complexity of the velocity field.

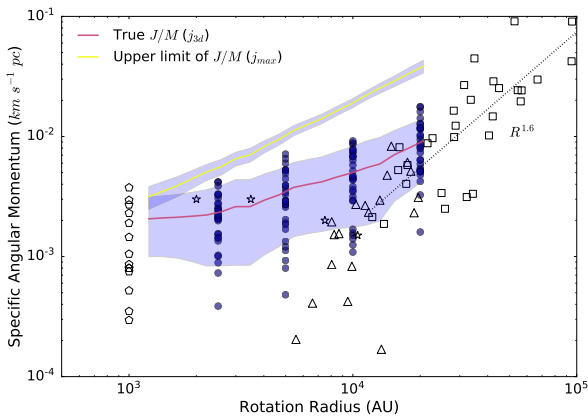


Figure 6. Comparison of the true angular momenta with the velocity gradient estimates, now assuming simple density weighting to construct the moment 1 map. The results are very similar to the radiative transfer results (cf. Fig. 3)

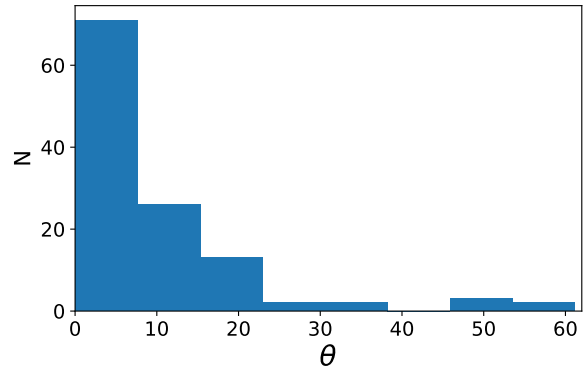
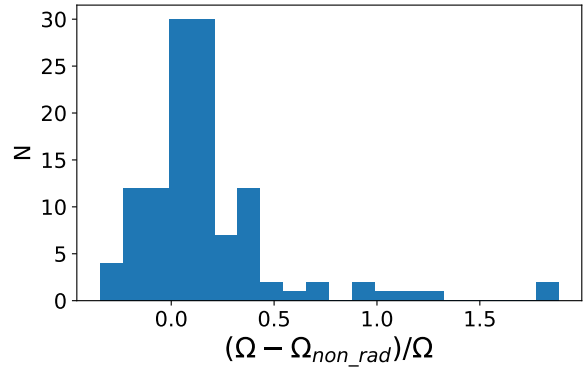


Figure 7. Upper: The distribution of relative difference between the all velocity gradient results (for ten cores in MHD run on four scales and three projections) after radiative transfer and without radiative transfer. The difference of 96% of projections is within a factor of two. Lower: the distribution of the difference between position angle of the velocity gradient after radiative transfer and without radiative transfer for the same data above. Most (about 90%) of the projections differ by less than 30 degrees.

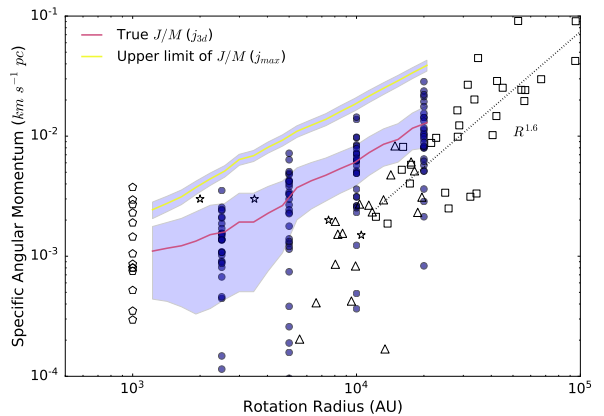


Figure 8. The comparison of j_{2d} and j_{3d} for non-magnetic field runs. While the behavior is similar to that of the MHD run, the non-magnetic case exhibits some very small values in projection, mostly for the very small masses of some of the sinks in the non-magnetic run (Table 1).

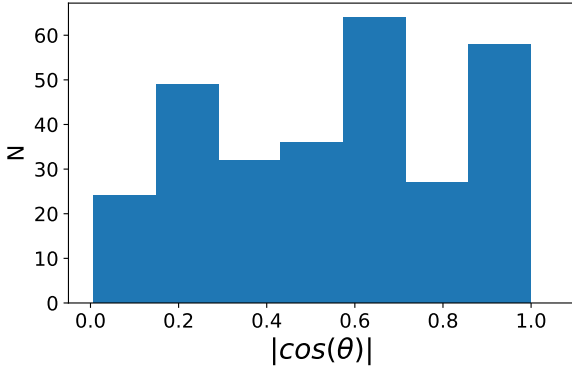


Figure 9. Histogram of $\cos\theta$, where θ is the angle between j_{3d} and x-axis (the direction of initial B-field). The orientation of the j_{3d} is consistent with a random distribution.

Conversely, we find that for certain projections our “observed” specific angular momenta can be an order of magnitude lower than the true values. We interpret this quite simply as the result of the orientation of the line of sight to the angular momentum vector, which occasionally should be unfavorable. This is another area in which we differ from the Dib *et al.* results, where there was no case in which the two-dimensional projection underestimated the true value of j .

These differing results emphasize the importance of understanding the nature of “turbulence” in molecular clouds. In our simulations, while there is an initial turbulent velocity field which seeds structure, at the later stages where we observe our cores, complex gravitational accelerations produced by the non-uniform density fluctuations and sinks are driving the motions. This scenario is consistent with the results of Seifried *et al.* (2018), who performed large-scale numerical simulations of molecular clouds created and perturbed by external supernovae. Seifried *et al.* found that the initial turbulence created during cloud formation decays rapidly as the cloud becomes more massive, concluding that SNe are generally not able to sustain observed molecular cloud turbulence. Our simulations therefore may be more realistic than those with continuously injected turbulence by an unspecified mechanism.

The motivation for simulating core formation and collapse in large-scale simulations is to allow the initial conditions - the angular momentum and the detailed velocity field - to develop naturally. Our results and those of other simulations on molecular cloud scales may be helpful in providing more realistic initial conditions for small-scale simulations of individual cores such as the recent investigations by Matsumoto *et al.* (2017) and Lewis & Bate (2018). For example, Matsumoto *et al.* (2017) suggest that $j \propto r^{3/2}$ is to be expected from turbulence, which is considerably different from what we find in our simulations. More large-scale simulations are needed with a wider variety of global initial conditions to explore this further.

5 CONCLUSIONS

We have analyzed the results of numerical simulations of star formation with and without magnetic fields with de-

caying turbulence, with and without radiative transfer post-processing. Using the same methods as typically used to observationally estimate specific angular momenta j for protostellar cores, we find that even though the assumption in these methods of uniform rotation and simple power-law density distributions are not correct in detail, the methods can still serve to produce estimates of j that are within a factor of two to three of the real values. These results are in contrast with other findings in cases where the turbulence is continually driven by an unspecified mechanism.

Our simulations do not include stellar feedback. Outflows from low-mass protostars pose a particular challenge to distinguish expansion from undisturbed core velocity fields (e.g., Tobin *et al.* 2011), which can dominate uncertainties in estimating core angular momenta. Simulations including schematic bipolar outflows could help constrain these uncertainties. In any case, our results suggest that it is worthwhile and important to continue observational efforts to estimate angular momenta of protostellar cores, especially given the significance of such studies for understanding the formation of protoplanetary disks.

ACKNOWLEDGMENTS

We acknowledge a helpful and timely report from an anonymous referee. This work used computational resources and services provided by Advanced Research Computing at the University of Michigan, Ann Arbor; and IRyA-UNAM, México. We used `matplotlib` Hunter (2007) and `numpy` Van Der Walt *et al.* (2011) for plotting and analysis. This work was supported in part by the University of Michigan and CONA-CyT grant number 255295.

REFERENCES

- Aikawa Y., Herbst E., 1999, *A&A*, **351**, 233
Aso Y., *et al.*, 2015, *ApJ*, **812**, 27
Ballesteros-Paredes J., Hartmann L. W., Vázquez-Semadeni E., Heitsch F., Zamora-Avilés M. A., 2011, *MNRAS*, **411**, 65
Belloche A., 2013, in Hennebelle P., Charbonnel C., eds, *EAS Publications Series Vol. 62*, *EAS Publications Series*. pp 25–66 ([arXiv:1305.0627](https://arxiv.org/abs/1305.0627)), doi:10.1051/eas/1362002
Belloche A., André P., 2004, *A&A*, **419**, L35
Belloche A., André P., Despois D., Blinder S., 2002, *A&A*, **393**, 927
Brinch C., Hogerheijde M. R., 2010, *A&A*, **523**, A25
Caselli P., Benson P. J., Myers P. C., Tafalla M., 2002, *ApJ*, **572**, 238
Dapp W. B., Basu S., Kunz M. W., 2012, *A&A*, **541**, A35
Dib S., Hennebelle P., Pineda J. E., Csengeri T., Bontemps S., Audit E., Goodman A. A., 2010, *ApJ*, **723**, 425
Federrath C., Banerjee R., Clark P. C., Klessen R. S., 2010, *ApJ*, **713**, 269
Federrath C., Sur S., Schleicher D. R. G., Banerjee R., Klessen R. S., 2011, *ApJ*, **731**, 62
Field G. B., 1965, *ApJ*, **142**, 531
Fryxell B., *et al.*, 2000, *ApJS*, **131**, 273
Ginsburg A., Robitaille T., Beaumont C., 2016, *psextractor*: Position-Velocity Diagram Extractor, *Astrophysics Source Code Library* (ascl:1608.010)
Goodman A. A., Benson P. J., Fuller G. A., Myers P. C., 1993, *ApJ*, **406**, 528

- Hartmann L., Ballesteros-Paredes J., Bergin E. A., 2001, *ApJ*, **562**, 852
- Heitsch F., Slyz A. D., Devriendt J. E. G., Hartmann L. W., Burkert A., 2006, *ApJ*, **648**, 1052
- Hunter J. D., 2007, *Computing In Science & Engineering*, 9, 90
- Joos M., Hennebelle P., Ciardi A., 2012, *A&A*, **543**, A128
- Joos M., Hennebelle P., Ciardi A., Fromang S., 2013, *A&A*, **554**, A17
- Koyama H., Inutsuka S. I., 2000, *ApJ*, **532**, 980
- Koyama H., Inutsuka S. I., 2002, *ApJ*, **564**, L97
- Krumholz M. R., Crutcher R. M., Hull C. L. H., 2013, *ApJ*, **767**, L11
- Landman D. A., Roussel-Dupre R., Tanigawa G., 1982, *ApJ*, **261**, 732
- Lewis B. T., Bate M. R., 2018, *MNRAS*, **477**, 4241
- Lewis B. T., Bate M. R., Price D. J., 2015, *MNRAS*, **451**, 288
- Li Z.-Y., Banerjee R., Pudritz R. E., Jørgensen J. K., Shang H., Krasnopolsky R., Maury A., 2014, *Protostars and Planets VI*, pp 173–194
- Masson J., Chabrier G., Hennebelle P., Vaytet N., Commerçon B., 2016, *A&A*, **587**, A32
- Matsumoto T., Machida M. N., Inutsuka S.-i., 2017, *ApJ*, **839**, 69
- Mestel L., 1963, *MNRAS*, **126**, 553
- Myers P. C., Benson P. J., 1983, *ApJ*, **266**, 309
- Offner S. S. R., Klein R. I., McKee C. F., 2008, *ApJ*, **686**, 1174
- Ohashi N., et al., 2014, *ApJ*, **796**, 131
- Oya Y., Sakai N., López-Sepulcre A., Watanabe Y., Ceccarelli C., Lefloch B., Favre C., Yamamoto S., 2016, *ApJ*, **824**, 88
- Robitaille T., Ginsburg A., Beaumont C., Leroy A., Rosolowsky E., 2016, spectral-cube: Read and analyze astrophysical spectral data cubes, Astrophysics Source Code Library (ascl:1609.017)
- Santos-Lima R., de Gouveia Dal Pino E. M., Lazarian A., 2012, *ApJ*, **747**, 21
- Santos-Lima R., de Gouveia Dal Pino E. M., Lazarian A., 2013, *MNRAS*, **429**, 3371
- Seifried D., Banerjee R., Pudritz R. E., Klessen R. S., 2012, *MNRAS*, **423**, L40
- Seifried D., Banerjee R., Pudritz R. E., Klessen R. S., 2013, *MNRAS*, **432**, 3320
- Seifried D., Walch S., Haid S., Girichidis P., Naab T., 2018, *ApJ*, **855**, 81
- Takakuwa S., et al., 2017, preprint, ([arXiv:1711.00447](https://arxiv.org/abs/1711.00447))
- Tobin J. J., et al., 2011, *ApJ*, **740**, 45
- Tobin J. J., Hartmann L., Chiang H.-F., Wilner D. J., Looney L. W., Loinard L., Calvet N., D'Alessio P., 2012, *Nature*, **492**, 83
- Truelove J. K., Klein R. I., McKee C. F., Holliman II J. H., Howell L. H., Greenough J. A., 1997, *ApJ*, **489**, L179
- Turk M. J., Smith B. D., Oishi J. S., Skory S., Skillman S. W., Abel T., Norman M. L., 2011, *ApJS*, **192**, 9
- Van Der Walt S., Colbert S. C., Varoquaux G., 2011, preprint, ([arXiv:1102.1523](https://arxiv.org/abs/1102.1523))
- Vaytet N., Commerçon B., Masson J., González M., Chabrier G., 2018, preprint, ([arXiv:1801.08193](https://arxiv.org/abs/1801.08193))
- Waagan K., Federrath C., Klingenberg C., 2011, *Journal of Computational Physics*, **230**, 3331
- Wolfire M. G., Hollenbach D., McKee C. F., Tielens A. G. G. M., Bakes E. L. O., 1995, *ApJ*, **443**, 152
- Wünsch R., Walch S., Dimbier F., Whitworth A., 2018, *MNRAS*, **475**, 3393
- Wurster J., Price D. J., Bate M. R., 2016, *MNRAS*, **457**, 1037
- Wurster J., Price D. J., Bate M. R., 2017, *MNRAS*, **466**, 1788
- Yen H.-W., Koch P. M., Takakuwa S., Ho P. T. P., Ohashi N., Tang Y.-W., 2015, *ApJ*, **799**, 193
- Zamora-Avilés M., Vázquez-Semadeni E., Körtgen B., Banerjee R., Hartmann L., 2018, *MNRAS*, **474**, 4824

This paper has been typeset from a $\text{\TeX}/\text{\LaTeX}$ file prepared by the author.